International Journal of Plasticity 144 (2021) 103022

Contents lists available at ScienceDirect

International Journal of Plasticity

journal homepage: www.elsevier.com/locate/ijplas

Strain partitioning enables excellent tensile ductility in precipitated heterogeneous high-entropy alloys with gigapascal yield strength

Feng He [a,b,**], Zhongsheng Yang [a], Shaofei Liu [b], Da Chen [b], Weitong Lin [b], Tao Yang [c], Daixiu Wei [d], Zhijun Wang [a,***], Jincheng Wang [a,****], Ji-jung Kai [b,e,*]

[a] State Key Laboratory of Solidification Processing, Northwestern Polytechnical University, Xi'an, 710072, PR China
[b] Centre for Advanced Nuclear Safety and Sustainable Development, City University of Hong Kong, Hong Kong, China
[c] Department of Materials Science and Engineering, City University of Hong Kong, Hong Kong, China
[d] Institute for Materials Research, Tohoku University, 2-1-1 Katahira, Sendai, Miyagi, 980-8577, Japan
[e] Department of Mechanical Engineering, City University of Hong Kong, Hong Kong, China

ARTICLE INFO

Keywords:
High entropy alloys
Heterogeneous structure
Mechanical properties
Deformation mechanism

ABSTRACT

High entropy alloys (HEAs) with grain-scale heterogeneous structure and coherent precipitates have shown gigapascal strength and considerable ductility. However, the origins of the excellent ductility of the HEAs with both precipitates and grain-scale heterogeneous structures are relatively less explored and not well understood. It is also still challenging to obtain such precipitated heterogeneous HEAs through efficient and economical thermomechanical processing procedures. Here, through single-step heat treatment, we developed a $Ni_2CoCrFeTi_{0.24}Al_{0.2}$ HEA with an excellent yield strength of ~1.3 GPa and tensile elongation of ~20%. Using multiple length-scale microstructure characterizations and micro-digital image correlation analysis, we revealed the strengthening and toughening mechanisms of the novel HEA. Our results showed that the grain-scale heterogeneous structure with $L1_2$ precipitates ranging from ~10 to 100 nm is responsible for the excellent strength-ductility combination. The good ductility is attributed to the strain-partitioning-induced additional deformation modes, i.e., deformation twinning and micro-bands, as well as the efficient hetero-deformation induced strain hardening effect. The superior yield strength is mainly due to the effective combination of precipitation hardening and dislocation strengthening. These findings not only provide a facile route to develop strong and ductile alloys but also deepen the understanding of the deformation mechanism of hetero-structured materials.

* Corresponding author. Centre for Advanced Nuclear Safety and Sustainable Development, City University of Hong Kong, Hong Kong, China.
** Corresponding author. State Key Laboratory of Solidification Processing, Northwestern Polytechnical University, Xi'an, 710072, PR China.
*** Corresponding author.
**** Corresponding author.
E-mail addresses: fhe224@cityu.edu.hk (F. He), zhjwang@nwpu.edu.cn (Z. Wang), jchwang@nwpu.edu.cn (J. Wang), jijkai@cityu.edu.hk (J.-j. Kai).

https://doi.org/10.1016/j.ijplas.2021.103022
Received 15 February 2021; Received in revised form 27 April 2021; Accepted 30 April 2021
Available online 3 June 2021

1. Introduction

Strong and ductile materials are the endless pursuit of metallurgists for the ecological, economic, and safety considerations. High-entropy alloys (HEAs) with complex compositions have attracted broad scientific attention for excellent mechanical and functional properties (Chung et al., 2019; George et al., 2019; Hua et al., 2021; Li et al., 2020c; Miracle and Senkov, 2017; Zhang et al., 2020b). The face-centered-cubic (FCC) HEAs have shown excellent toughness at wide temperature and strain rate ranges (Gludovatz et al., 2014). It is unsatisfying, however, that the yield strengths of single-phase FCC HEAs are far away from structural application requirements (George et al., 2020; Zhang et al., 2014). Two routes with different emphasis, i.e., compositional screening and thermal-mechanical processing (TMP) design, have been followed to improve the mechanical properties of FCC HEAs. The composition screening aims to thermodynamically change the microstructure, leading to solid solution strengthening (Toda-Caraballo and Rivera-Díaz-del-Castillo, 2015), metastable engineering (Li et al., 2017; Wei et al., 2018, 2019), and precipitation hardening (He et al., 2016, 2019; Li et al., 2020a; Liu et al., 2016; Sadeghilaridjani et al., 2020; Chen et al., 2019; Fan et al., 2020). The TMP design mainly focuses on controlling kinetic behaviors of materials, which usually results in grain refinement (Liu et al., 2013; Schneider et al., 2020), dislocation hardening (He et al., 2018b; Jo et al., 2017; Zheng et al., 2021), and hetero-deformation induced (HDI) strain hardening (Ma and Wu, 2019; Ma et al., 2018; Yang et al., 2018a). Both routes have efficiently improved the comprehensive mechanical properties of FCC HEAs through specific strengthening mechanism, e. g. a careful composition screening increased the yield strength of NiCoFe to gigapascal level through precipitation hardening (Yang et al., 2018b), and smart TMP design also enhanced the yield strength of NiCoCr to ~ 1 GPa utilizing HDI hardening (Yang et al., 2018a). In addition, Su et al. (2019) showcased that a TMP-design induced hierarchical microstructure also considerably improved the mechanical properties of metastable HEAs.

Since the precipitation hardening and HDI hardening have separately shown excellent strengthening effects, extensive efforts have been made to utilize them to develop strong and ductile HEAs comprehensively. In the $Co_{35}Ni_{20}Fe_{20}Cr_{15}Mo_{10}$ HEA (Ming et al., 2017), the solid solution hardening, nanotwins (fine grain size), and precipitation hardening were effectively combined by cold rolling and annealing. Similar studies have also been conducted in $NiCoCrFeAl_x$ (He et al., 2020; Hou et al., 2020), $Ni_{2.1}CoCrFeNb_{0.2}$ (Sunkari et al., 2020), and $Ni_{1.5}Co_{1.5}CrFeTi_xAl_y$ (Nandal et al., 2021). However, a large amount of brittle intermetallic phases formed in these HEAs, leading to moderate strengthening effects. More recently, Zhang et al. (2020a) coupled the precipitation hardening and HDI hardening in $Fe_{42.26}Ni_{27.5}Co_{17.5}Al_{10.5}Ta_{2.2}$, in which the coherent γ' precipitates and heterogeneous structure were obtained. This kind of dual heterogeneous structures was also reported in a Ni–Co–Cr HEA (Du et al., 2020). Both HEAs with efficient precipitation hardening and HDI hardening showed excellent strength and ductility synergy, demonstrating a promising path to develop ultra-strong and ductile HEAs as well as traditional alloys (Niendorf et al., 2013; Slone et al., 2018; Sohn et al., 2017; Zhang et al., 2018). Nevertheless, the good mechanical performance of these HEAs heavily relied on complex TMP procedures, including hot rolling, cryogenic-temperature rolling, room-temperature rolling, and two/three-step annealing (Du et al., 2020; Zhang et al., 2020a). More importantly, the underlying origin of the excellent ductility in those HEAs with both high-content precipitates and high-density dislocations are still an open issue.

In light of the above two issues, we in the present study developed an ultra-strong and ductile $Ni_2CoCrFeTi_{0.24}Al_{0.2}$ HEA through single-step heat treatment. With the aid of X-ray diffraction (XRD), scanning electron microscope (SEM), electron backscattered diffraction (EBSD), and transmission electron microscope (TEM), the microstructure and deformation mechanisms of the novel HEA were systematically investigated across multiple length scales. Particularly, an in-situ SEM study was carried out for micro-digital image correlation (μ-DIC) analysis to reveal the strain partitioning behaviors between different regions of the hetero-structured HEA. The results show that severe strain partitioning leads to deformation twinning and micro-bands, which were rarely observed in homogeneous precipitation-hardened HEAs, in the current $Ni_2CoCrFeTi_{0.24}Al_{0.2}$ HEA. Then, the correlation between strain partitioning and ductility was discussed.

2. Experimental methods

2.1. Material preparation

The novel $Ni_2CoCrFeTi_{0.24}Al_{0.2}$ HEA was developed by considering both the phase stability of precipitates and the kinetics of concurrent recrystallization and precipitation behaviors (Supplementary Note 1). Samples with the nominal composition of $Ni_2CoCrFeTi_{0.24}Al_{0.2}$ were produced by arc-melting a mixture of high-purity raw elements (>99.9 wt %) in a Ti-gettered argon atmosphere. The ingots were remelted at least four times to promote the chemical homogeneity and then dropped into a water-cooled copper mould with the dimension of $50 \times 10 \times 5$ mm^3. The alloys were first solid solution treated at 1200 °C for 2 h followed by water quenching and then cold-rolled along the longitudinal direction with a total thickness reduction of ~70%. The final rolled plates were subsequently annealed at 800 °C from 15 min to 120 min in air and then quenched in water.

2.2. Mechanical testing

Dog-bone-shaped specimens with a gauge dimension of $12.5 \times 1.2 \times 3$ mm^3 were fabricated by electron-discharge machining for tensile tests. The longitudinal (tensile) axes of the specimens were aligned with the rolling direction of the original plate, and the faces were parallel to the plate. Tensile specimens were polished on the faces and sides of the gauge section using 240-, 800-, and 1500-grit SiC paper. Uniaxial tensile tests were carried out on a TSMT testing machine (TSMT EM6. 504) with a strain rate of 1×10^{-3} s^{-1} at ambient temperature. Five loading-unloading-reloading (LUR) cycles were conducted during the LUR test, the specimen was firstly

stretched to a designated strain (i. e., 2%) at a strain rate of $1 \times 10^{-3}\cdot s^{-1}$, and then unloaded by the stress-control mode to 50 MPa at the unloading rate of 10 MPa s^{-1}, followed by reloading at a strain rate of $1 \times 10^{-3}\cdot s^{-1}$ to the same applied stress before the next unloading. An extensometer (YYJ, Sanjing Co., Ltd) was used for both the quasi-static tensile and LUR tests.

2.3. Microstructure characterization

The XRD was carried out from 20 to 100° on Rigakud/max2550 with Cu radiation. A monochromator was used to filter the K_{β}, and Jade 5.0 was used to analyze the phases from XRD patterns. Microstructure characterization was carried out via scanning electron microscope (SEM, Tescan MIRA3) and transmission electron microscope operating at 200 keV (TEM, JEOL 2100 F equipped with X Energy Dispersive Spectrometry). For the SEM analysis, samples were prepared by grinding, polishing in diamond suspension, and final polishing in colloidal silica suspension. The recrystallization microstructure was studied using the HKL-Technology electron backscattered scattering diffraction (EBSD) system from the Oxford Instruments. For the TEM analysis, the sheet specimens were firstly mechanically ground to a thickness below 100 μm using SiC paper, and then the samples were punched into 3-mm-diameter discs and further thinned by twin-jet electro-polishing to a thickness of electron transparency.

2.4. Local strain measurement via micro-digital image correlation (DIC)

The in-situ tensile test specimens were prepared by Electrical Discharge Machining (EDM) with a gauge dimension of $4 \times 2 \times 1$ mm^3. Before testing, the surfaces of the specimens were prepared by fine grinding and diamond polishing, followed by colloidal silica (particle size of 40 nm). Then, a monolayer of SiO_2 particles (40 nm in size) was homogeneously dispersed on the sample surface for local strain field measurements. In-situ deformation was carried out at a crosshead speed of 4 μm/min using a Kammrath & Weiss micro-test system equipped with a 5 kN load cell. In-beam SE detector was used at 20 kV acceleration voltage to capture the high-resolution (16,384 × 16,384) images of the ROI with SiO_2 particles. These images were taken at the strain of 0, 1.5%, 6%, 9%, 12%, respectively. The recorded images were analyzed using GOM Correlate software (https://www.gom.com/3d-software/gom-correlate.html) to obtain strain maps at different strain levels. The facet size of 60 × 60 pixels was used when we create the

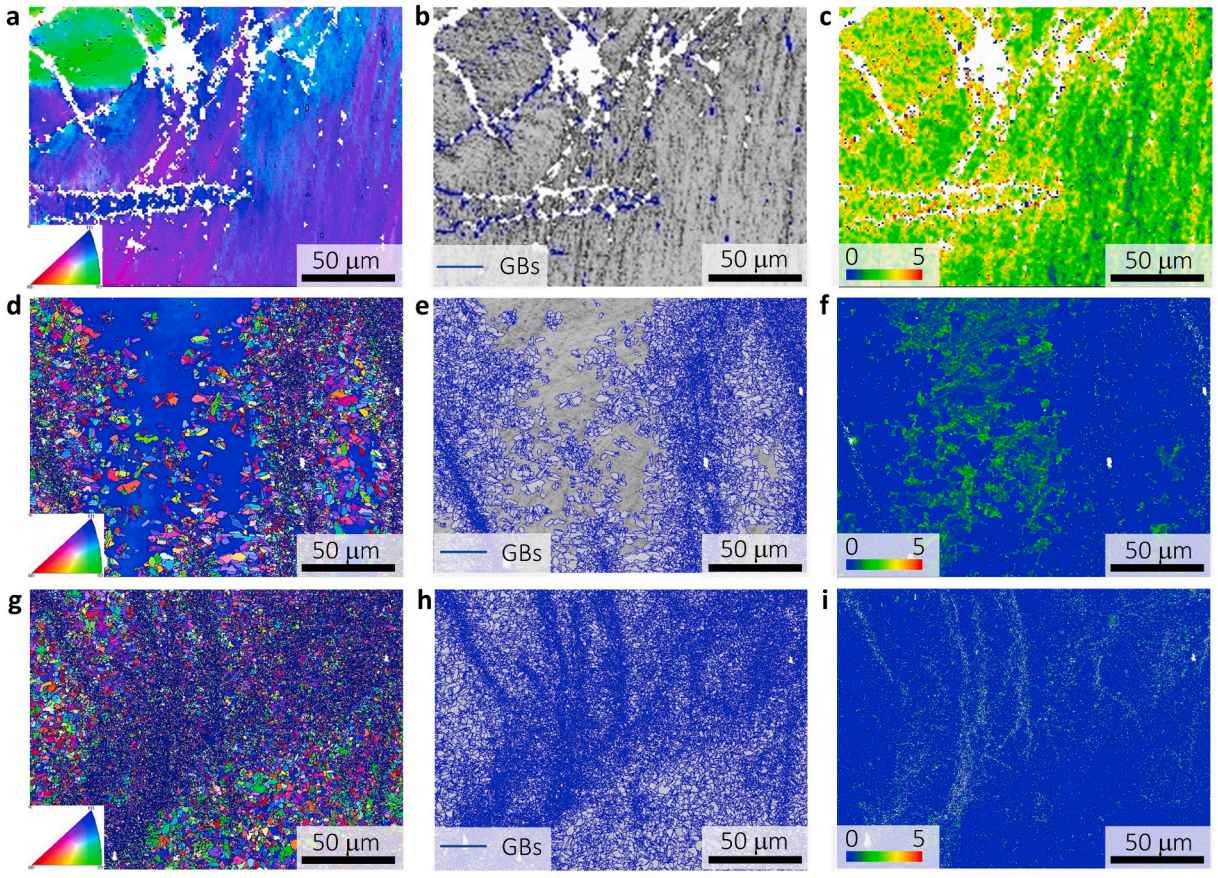

Fig. 1. The IPF, IQ, and KAM maps of 70%-rolled $Ni_2CoCrFeTi_{0.24}Al_{0.2}$ annealed at 800 °C for different times; (a–c) 60 min, (d–f) 90 min, and (g–i) 120 min.

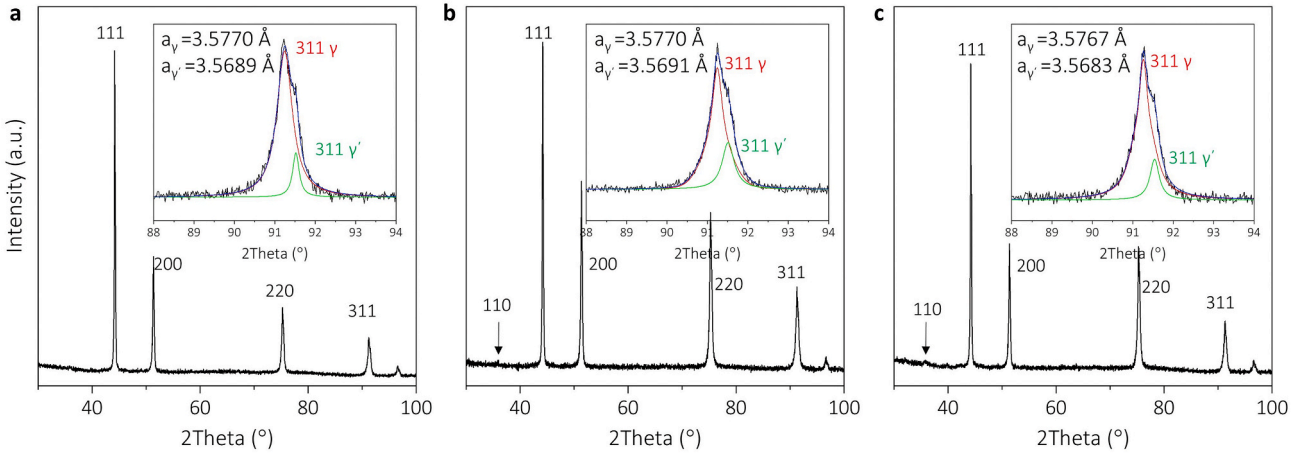

Fig. 2. XRD patterns of 70%-rolled $Ni_2CoCrFeTi_{0.24}Al_{0.2}$ annealed at 800 °C for different time; (a) 60 min, (b) 90 min, and (c) 120 min.

surface component using GOM correlate software, resulting in a spatial resolution of the strain map to be 1.6 × 1.6 μm^2. Since the different regions in the analyzed area are larger than 16 × 16 μm^2 (Fig. 7a), the spatial resolution is high enough to reveal the strain partitioning in the current study.

3. Results

3.1. Grain-scale heterogeneous structure

Fig. 1 showed the EBSD results of $Ni_2CoCrFeTi_{0.24}Al_{0.2}$ annealed for 60, 90, and 120 min at 800 °C, respectively. The inverse pole figure (IPF) image in Fig. 1a shows a single crystal orientation (similar color) with large local misorientations (notable color change). The image quality (IQ) map (Fig. 1b) and the kernel average misorientation (KAM) map (Fig. 1c) further confirmed the absence of high angle grain boundaries and the existence of high local misorientations inside the grain. These results jointly revealed that the HEA was not recrystallized after annealed for 60 min (hereafter we note this sample as non-recrystallized). A notable change in microstructure was observed in the sample that was annealed for 90 min, as shown in Fig. 1d–f. Many small grains were detected by IPF and IQ images in Fig. 1d and e. Apart from these small grains, a large area with the same crystal orientation was also observed. The KAM map in Fig. 1f showed that there is little local misorientation in the small grain areas while relatively high local misorientation in the rest areas. These features verified a typical partially recrystallized microstructure with a recrystallization volume fraction of 55% (hereafter, we note

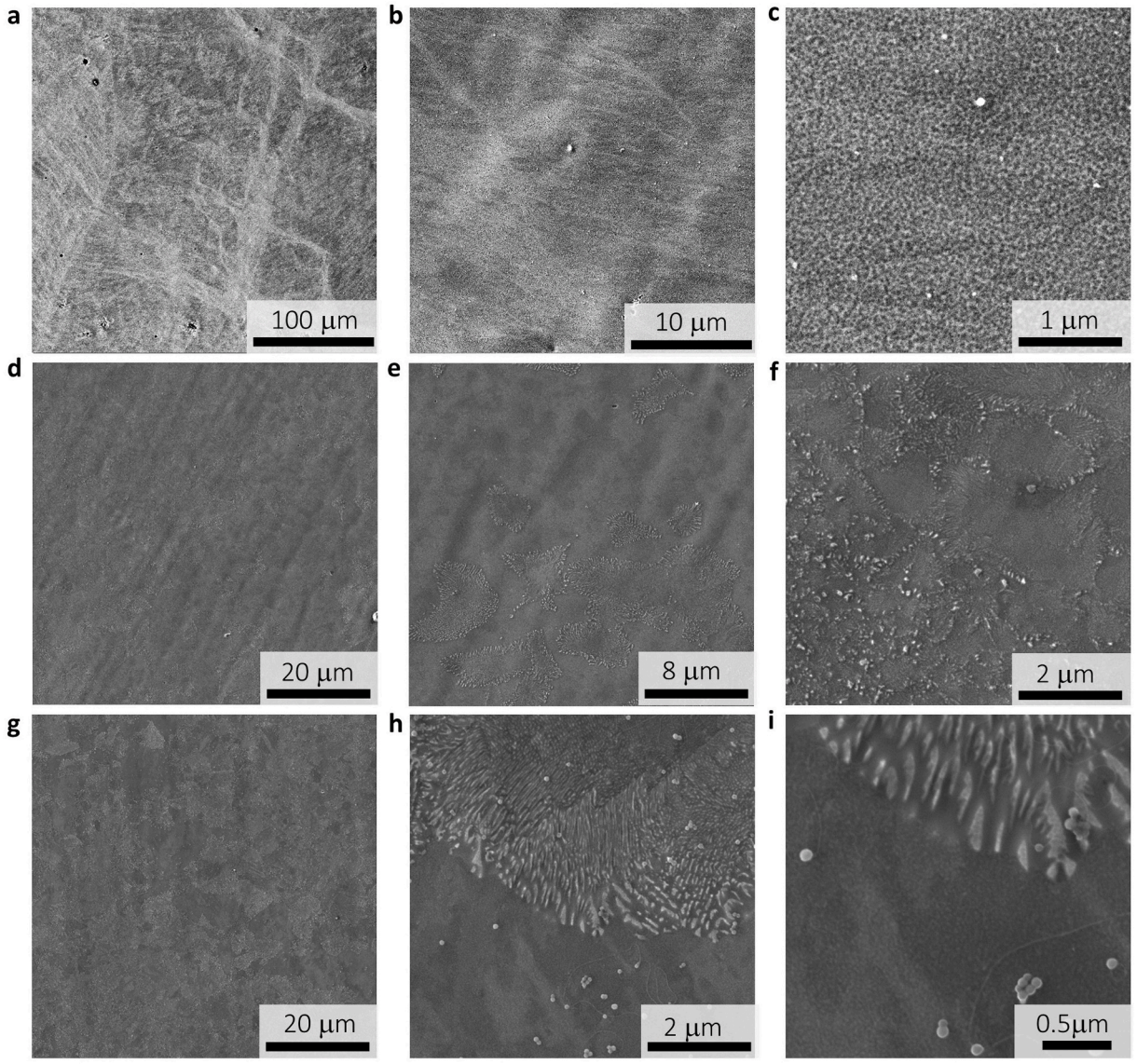

Fig. 3. SEM images of the 70%-rolled $Ni_2CoCrFeTi_{0.24}Al_{0.2}$ annealed at 800 °C for different time; (a–c) 60 min, (d–f) 90 min, and (g–i) 120 min.

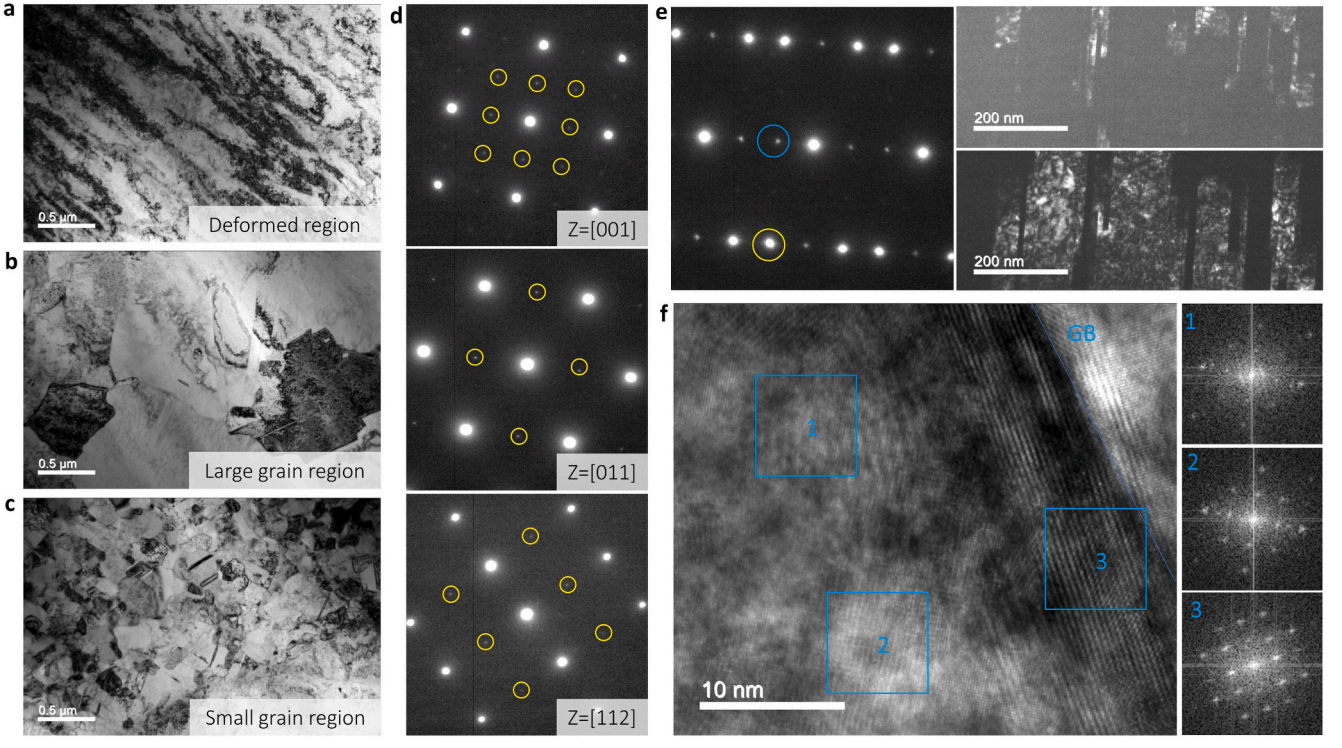

Fig. 4. TEM images of the partially recrystallized $Ni_2CoCrFeTi_{0.24}Al_{0.2}$ (annealed for 90 min at 800°c); (a) deformed region, (b) large grain region, (c) small grain region, (d) representative SADPs, (e) BF and DF images showing deformation twins and η phase, and (f) HRTEM image showing γ′ and η phases.

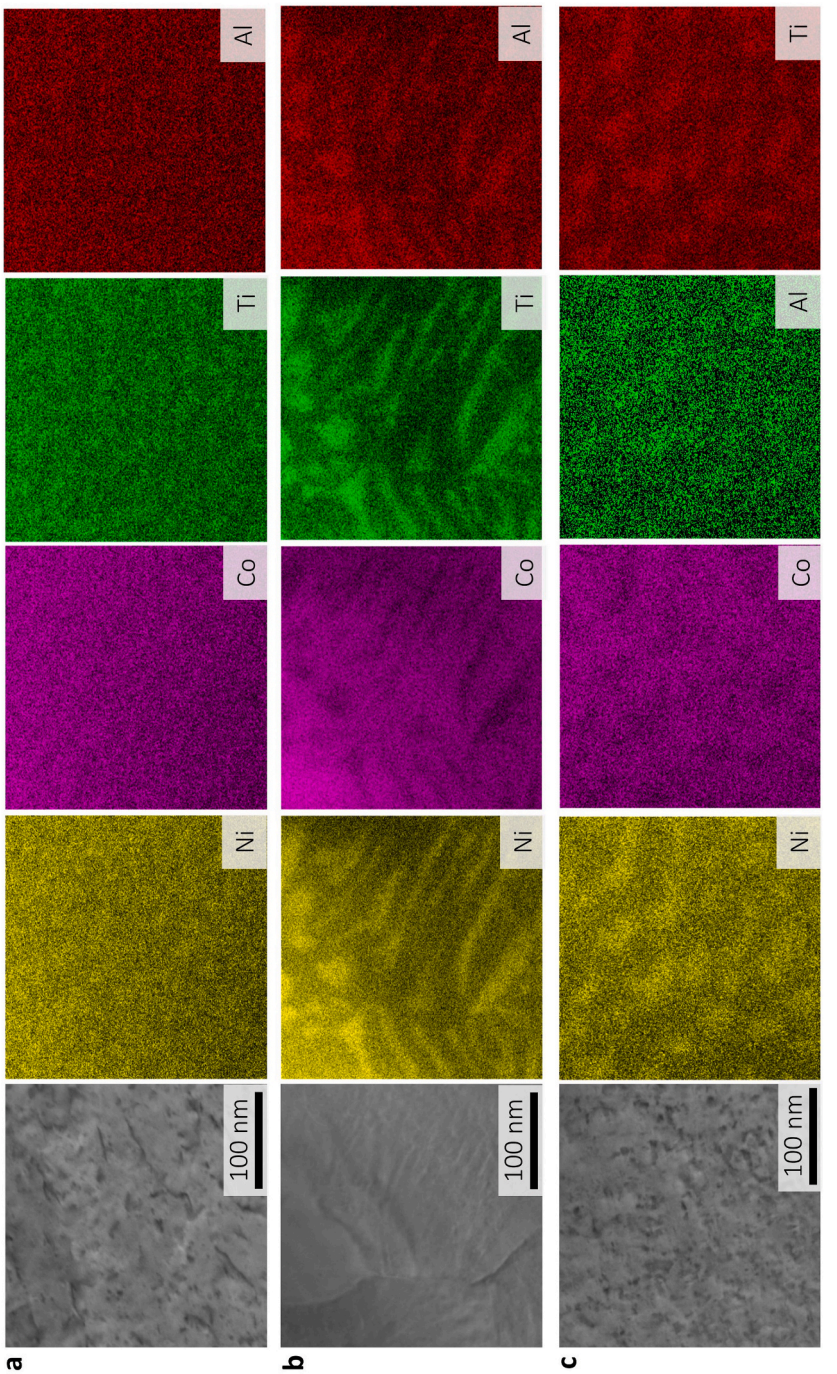

Fig. 5. STEM-EDS mapping of the deformed region (a), grain boundary region (b), and recrystallized region (c) of the partially recrystallized $Ni_2CoCrFeTi_{0.24}Al_{0.2}$ HEA.

this sample as partially-recrystallized HEA). Additionally, the local misorientation of the un-recrystallized region became lower when comparing the KAM maps in Fig. 1c and f, indicating that the degree of recovery also increased rapidly in this annealing stage. As the annealing time increased to 120 min, an almost fully recrystallized (97%) $Ni_2CoCrFeTi_{0.24}Al_{0.2}$ was observed in Fig. 1g–i. IPF and IQ mages showed randomly distributed small grains, and the KAM map shows the absence of local misorientation inside these grains. The quantitative analysis of grain boundary frequency in Fig. S3 also confirmed the evolution of recrystallization behaviors.

To reveal the precipitation behavior of these three HEAs in a grain scale, we carried out high-resolution XRD measurements and presented them in Fig. 2. A single set of typical FCC diffraction peaks was obtained for all three HEAs, while weak superlattice diffractions of (110) were also detected in the recrystallized samples (Fig. 2b and c). The diffraction peaks were further zoomed in to confirm the phase compositions of the HEAs carefully. It was found that all the FCC peaks are composed of two overlapped peaks. As an example, the enlarged (311) diffraction peaks were displayed as the insets. Together with the (110) peak, these diffraction peaks revealed the existence of $L1_2$ phase in the three HEAs. Using PsdVoigt fitting, the lattice parameters of the two phases were obtained. As shown in the insets, both the lattice parameters of γ and γ′ phases almost kept unchanged when the annealing time increased, indicating that there is no sharp composition change during this process. Han et al. (2018) have found that the chemical composition of the γ′ phase in the NiCoCrFe-based HEAs becomes stable when the aging time is higher than 60 min at 800 °C, coinciding with our results. The above results showed that not only a grain-scale heterogeneous structure but also a stable γ′ phase had been obtained in the partially recrystallized $Ni_2CoCrFeTi_{0.24}Al_{0.2}$.

3.2. Precipitates and nano-scale heterogeneity

SEM analysis was carried out to show the morphology of precipitates, as shown in Fig. 3. SEM images with different magnifications in Fig. 3a–c showed the randomly distributed nano-sized particles in the non-recrystallized samples (60 min annealed). Combining the XRD results in Fig. 2a, we can conclude that these precipitates are all γ′ phases with $L1_2$-type superlattice. Although precipitates occurred in a heavily deformed (70% cold rolled) sample, there is no third phase, e.g., η and B2 phases, that can be detected in the studied samples. Fig. 3d–f showed the precipitates in the partially recrystallized sample (annealed for 90 min) under the view field from a hundred to several micrometers. The precipitates were observed in both recrystallized and un-recrystallized regions, as shown in Fig. 3d. However, the shape of precipitates varied from that observed in Fig. 3c. Elongated particles distributed at the grain boundaries and the spherical particles inside the grain are larger than those in the deformed region (Fig. 3e and f). Although XRD measurements (Fig. 3b) did not detect other phases in this sample, it is hard to say that all these precipitates are γ′ phases since η phase with lathed shape has been reported (Tong et al., 2019). Similar results were obtained in the 120 min annealed sample, as shown in Fig. 3g–i.

To further understand the nano-scale microstructure of cold-rolled and annealed $Ni_2CoCrFeTi_{0.24}Al_{0.2}$, TEM analysis was carried out for a partially recrystallized sample. Fig. 4a – 4c showed the bright field (BF) images of different regions in the partially recrystallized sample. Consistent with the EBSD results in Fig. 1d and e, a deformed region with high dislocation density (Fig. 4a), a recrystallized region with relatively large grains (Fig. 4b), and a recrystallized region with tiny grains (Fig. 4c) were detected. The representative diffraction patterns from these three regions were presented in Fig. 4d. Superlattice spots (yellow circles) from three different incident axis collectively showed that the precipitates, including the elongated precipitates (DF image in Fig. S4), exhibit typical $L1_2$ crystal structure. This was in good agreement with XRD results and again confirmed that the γ′ phase in current $Ni_2CoCrFeTi_{0.24}Al_{0.2}$ is stable even during the concurrent precipitation and recrystallization process. Apart from γ′ phase, η phase (right upper image of Fig. 4e) and deformation twins (right lower image of Fig. 4e) were occasionally detected. The HRTEM image in Fig. 4f

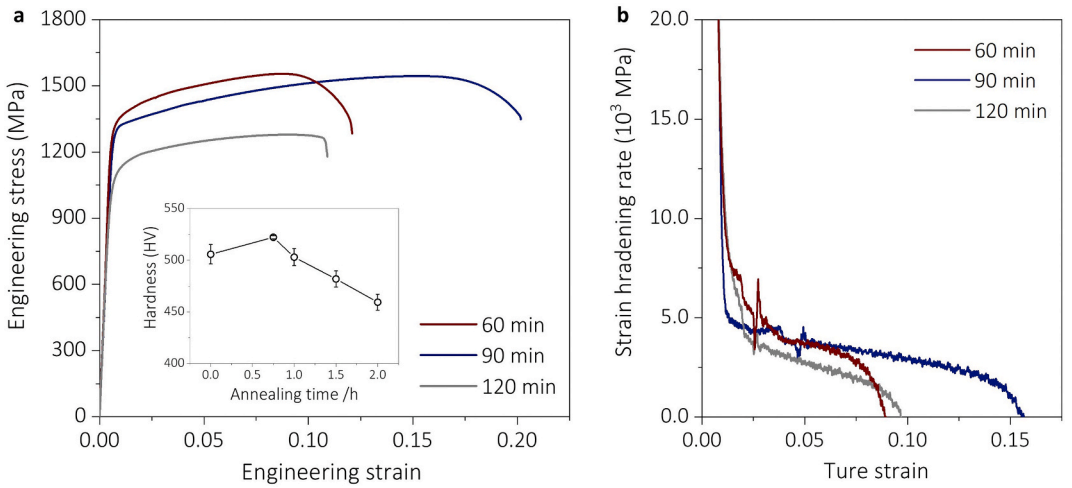

Fig. 6. (a) Tensile stress-strain curves of the 70%-rolled $Ni_2CoCrFeTi_{0.24}Al_{0.2}$ annealed at 800 °C for different times, and (b) corresponding strain hardening rate vs. true strain plots of (a).

further confirmed the existence of γ′ and a very small amount of η phases along the grain boundary.

The chemical compositions of the γ′ phase were characterized using STEM-EDS mapping. Fig. 5a – 5c separately showed the EDS mapping of the deformed region, grain boundary region, and recrystallized region. Precipitates from all three regions that are rich Ni, Ti, and Al, agreeing well with the composition of γ′ phase in previous studies (He et al., 2016). Comparing the γ′ phase in the different regions, we found that the γ′ phase at grain boundary has the largest particle size and elongated shape; these in the recrystallized grains show spherical shape with smaller size, and the γ′ phase in the deformed region is the smallest in size. Based on the TEM and SEM characterizations, the partially recrystallized $Ni_2CoCrFeTi_{0.24}Al_{0.2}$ consisted of γ′ phase with particle size ranging from 10 to 100 nm. Therefore, we successfully obtained a multi-scale heterogeneous structure with precipitates and defects through single-step cold rolling and annealing in the $Ni_2CoCrFeTi_{0.24}Al_{0.2}$ HEA.

3.3. Mechanical response

Fig. 6a showed tensile stress-strain curves of $Ni_2CoCrFeTi_{0.24}Al_{0.2}$ at different conditions. The partially recrystallized sample showed the best strength-ductility combination with a yield strength of ~1300 MPa, tensile strength of ~1540 MPa, and total

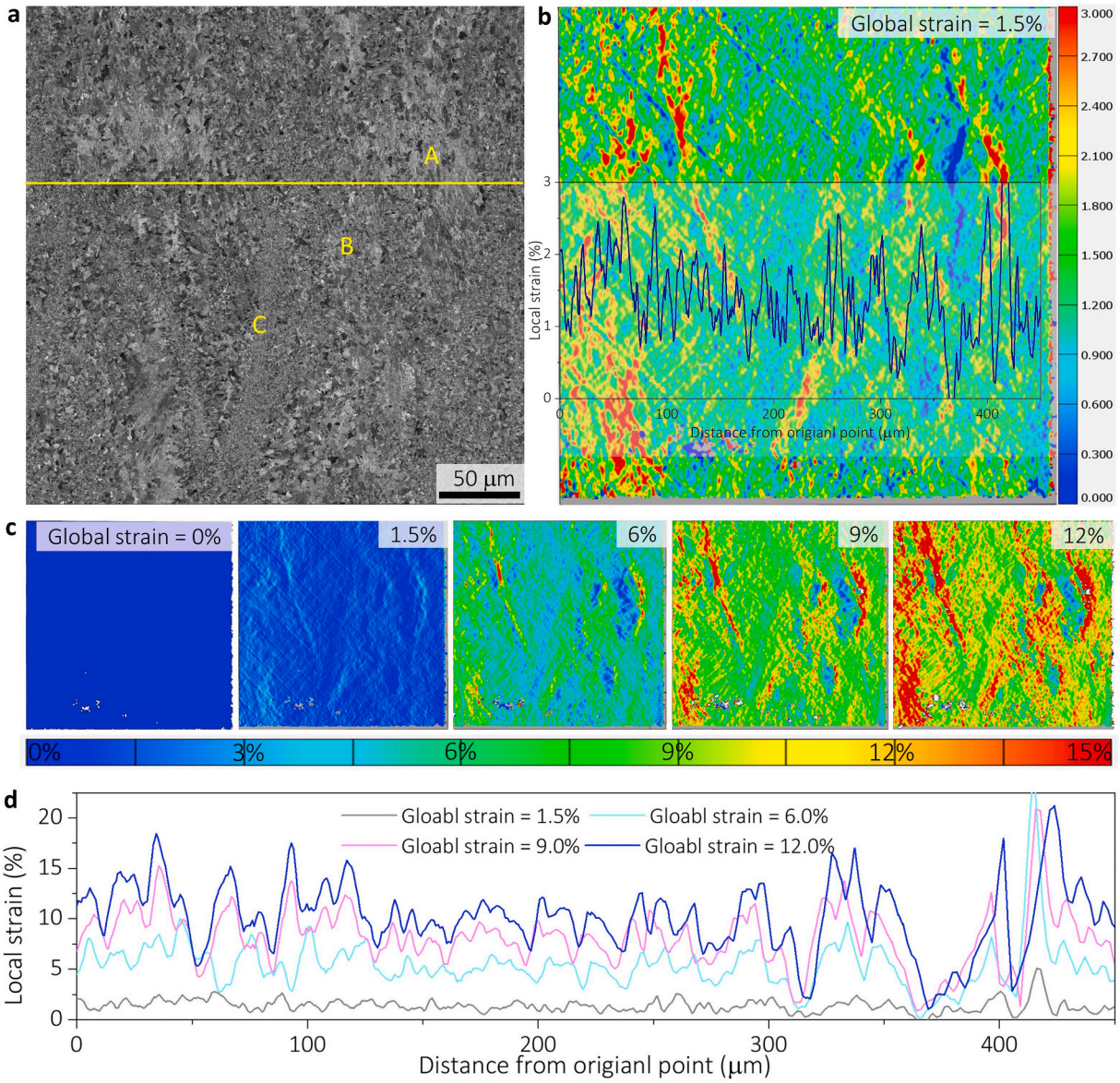

Fig. 7. (a) BSE image with different regions (A – deformed, B – large grain, C – small grain) of the region used for micro-DIC, (b) strain map and line profile of local strain along yellow line in (a) at a global strain of 1.5%, and (c) the evolution of strain partitioning as a function of global strain. (For interpretation of the references to color in this figure legend, the reader is referred to the Web version of this article.)

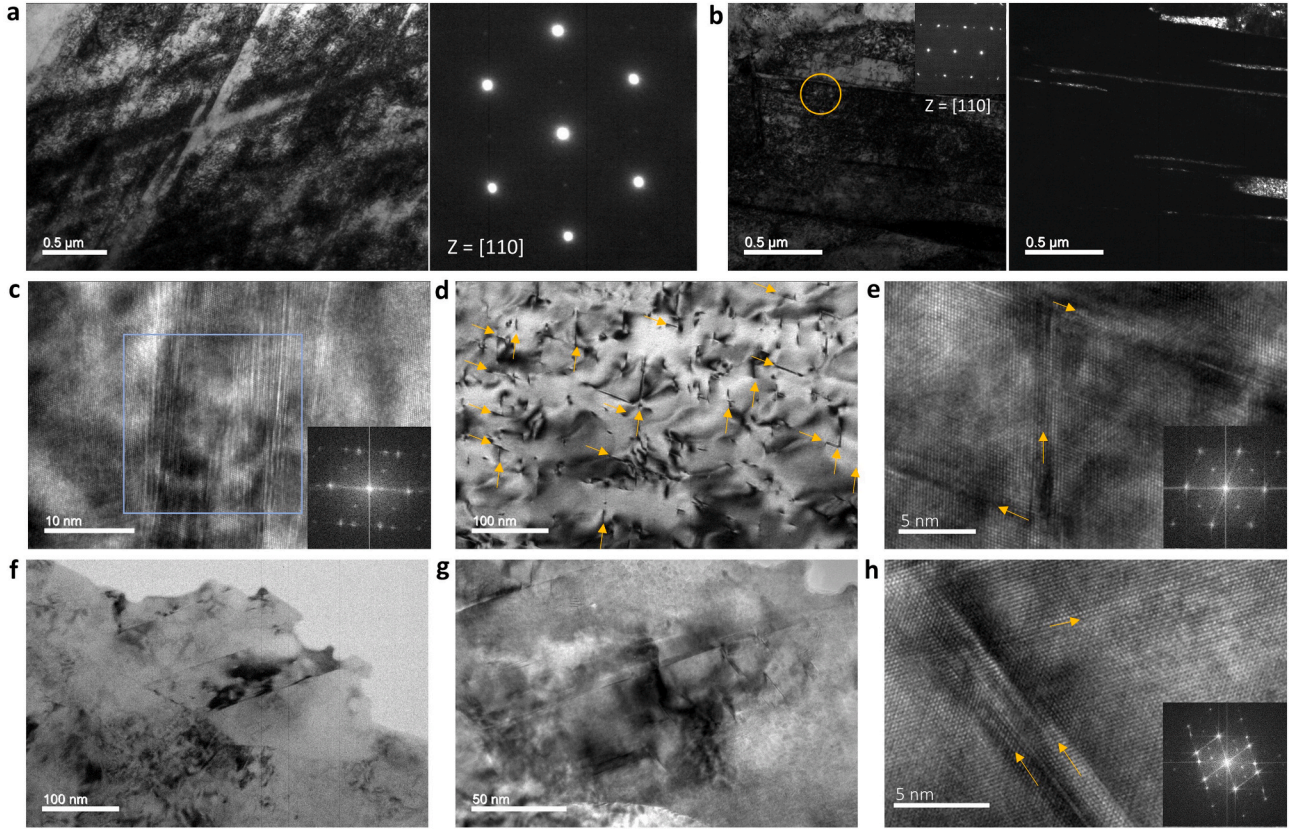

Fig. 8. TEM images of the fractured partially recrystallized $Ni_2CoCrFeTi_{0.24}Al_{0.2}$ (annealed for 90 min at 800°c); (a) BF and SADP images of the deformed region, (b) BF, SADP, and DF images of large grain region, (c) HRTEM image of deformation twins in large grain region, (d) BF images showing SFs in large grain region, (e) HRTEM image of SFs in (d), (f and g) BF images of a small grain, (h) HRTEM image showing SFs in small grain.

elongation of 0.2. The un-recrystallized sample exhibited a slightly higher yield strength (~1330 MPa), similar tensile strength (~1560 MPa), but lower ductility (0.13). When the recrystallization finished, both yield strength (1050 MPa), tensile strength (~1280 MPa), and ductility (0.11) became worse. This should be due to the coarsening of precipitates and the disappearance of grain-scale heterogeneous structures. Fig. 6b showed the strain hardening rate vs. true strain plots. The strain hardening rate of the partially recrystallized HEA reached 4.5 GPa at the initial stage of deformation and is always higher than 2.0 GPa during the uniform deformation stage. Consequently, despite the high yield strength, the partially recrystallized HEAs showed excellent tensile ductility. The hardness evolution as a function of annealing time was also presented as the inset of Fig. 6a. The hardness increased first and then decreased with annealing time, demonstrating the typical concurrent recrystallization and precipitation behaviors of $Ni_2CoCrFeTi_{0.24}Al_{0.2}$.

4. Analysis and discussion

4.1. Hetero-deformation induced strain hardening

It has been widely argued that the heterogeneous structure would produce strain hardening due to the strain partitioning between soft and hard regions (Hasan et al., 2019; Li et al., 2020b; Zhao et al., 2020). In the present study, as described earlier, the partially recrystallized $Ni_2CoCrFeTi_{0.24}Al_{0.2}$ HEAs exhibit a microstructure with grains ranging from sub-micrometers to hundreds of micrometers and precipitates ranging from ~10 to ~100 nm. Expectedly, this multi-scale multi-phase heterogeneous structure will provide more efficient strain partitioning. To unambiguously reveal the strain partitioning in the current heterostructured HEA, we present in Fig. 7 the strain map of partially recrystallized $Ni_2CoCrFeTi_{0.24}Al_{0.2}$ obtained from micro-DIC as a function of strain (images used for DIC is provided in Fig. S4). The BSE image in Fig. 7a showed that the selected area consists of deformed regions (as A represented), larger recrystallized grain regions (as B represented), and fine recrystallized grain regions (as C represented). Note that all these regions are composed of γ matrix and nano-sized γ′ precipitates with different sizes (Figs. 4 and 5), which would make the strain partitioning even complex. As shown in Fig. 7b, evident strain partitioning was observed at the beginning of plastic deformation. The large grain regions undertook the highest strain, followed by the small grain regions, while the deformed region almost kept undeformed. A line profile along the cross-section marked by the yellow line in Fig. 7a was given as the inset of Fig. 7b. At the global strain of 1.5%, the local strain of region B reached 3%, while that of region A is close to zero. The region C with fine recrystallized grains showed strain values close to macroscopic strain. Moreover, the strain distributions in the same regions are also nonuniform, especially for recrystallized regions. This should be owing to the heterogeneity in precipitates (Fig. 5 and S4), which resulted in the difference in precipitation hardening effect. Fig. 7c presented the evolution of the strain map as the global strain increased to 12%, and Fig. 7d showed the quantified evolution of strain distribution along the yellow line in Fig. 7a. The strain partitioning behavior existed during the whole plastic deformation and became more evident at high deformation levels. For example, the highest local strain is ~21%, and the lowest local strain is ~1% when the global strain is 12%.

This kind of strain partitioning positively influences the strain hardenability of the HEA from two aspects. One is that the strain localization stimulated extra deformation modes, and the other is that the severe strain partitioning resulted in effective HDI strain hardening. Fig. 8 showed the TEM images taken from different regions of the fractured partially recrystallized $Ni_2CoCrFeTi_{0.24}Al_{0.2}$. In the non-recrystallized regions, as shown in Fig. 8a, planar slip and microbands were the main features. The diffraction pattern from [110] zone axis indicated the absence of deformation twins. However, deformation twins were easily detected in the large grain regions, as shown in Fig. 8b. The BF images showed several grains with grain size larger than 1 μm and sharp contrast change inside the grains. With the help of SADP and DF images, we revealed that deformation twins occurred in the large grain regions after deformation. These twins are thin and usually stopped inside the grain, which is different from annealing twins. The HRTEM image was also obtained to show the features of deformation twins and presented in Fig. 8c. It can be found that the twin boundary is composed of SFs, instead of sharp crystal orientation in a single crystal plane (Laplanche et al., 2017). The FFT inset showed the twin boundary, and SFs cut through the precipitates. The DF and HRTEM images collectively both revealed these twins are nano-scaled with SFs at twin boundaries, indicating that they are mechanically induced twins during deformation. Apart from deformation twins, SFs were also widely observed inside the deformed large grains, as the arrows pointed in Fig. 8d. The straight and short lines with two different orientations are the typical feature of SFs, which are further confirmed by HRTEM and FFT images in Fig. 8e. In the small grain regions, deformation mode was mainly characterized by SFs, as shown in Fig. 8f– h. The BF image in Fig. 8f showed there are two twin boundaries in the small grain. The image with higher magnification showed that SFs exist near the twin boundary and inside the grains. Fig. 8h showed the HRTEM and FFT images, indicating a typical deformation feature of SFs.

As Fig. 8 demonstrated, the deformed partially recrystallized $Ni_2CoCrFeTi_{0.24}Al_{0.2}$ showed abundant deformation modes, which are different from that of the reported γ′ hardened HEAs. Previously, SFs were widely found at both room and cryogenic temperatures and believed to be the dominant deformation modes of γ′-hardened HEAs (Tong et al., 2019; Zhao et al., 2017). Sometimes, the microband was also observed at the later stage (true strain >0.3) of γ′-hardened HEAs and contributed to the strain hardening and ductility (Yang et al., 2018b). In the present study, apart from SFs, both deformation twins and micro-bands occurred during the tensile deformation of partially recrystallized $Ni_2CoCrFeTi_{0.24}Al_{0.2}$ (Fig. 8). Based on the strain partitioning analysis, we asserted that the strain localization in the large-grain area leads to higher stress and thus stimulates the deformation twinning (Fig. 8b). Additionally, since the deformed region consists of high dislocation density (Fig. 4a) and deforms at a very high strain/stress level (Fig. 7), it easily forms micro-bands (Bay et al., 1992; Yang et al., 2018b; Yoo and Park, 2008). These two additional deformation mechanisms, i.e., the deformation twinning and micro-bands, benefited the strain hardenability of the partially recrystallized $Ni_2CoCrFeTi_{0.24}Al_{0.2}$ HEA and thus led to good ductility.

The other positive effect of strain partitioning is on the HDI strain hardening effect (Liu et al., 2020; Wu et al., 2014). The load-unload-reload (LUR) test was used to measure the HDI hardening, as shown in Fig. 9. Obvious hysteresis loops were obtained at true strain from 0.02 to 0.1, and they became larger with the increase of true strain. The HDI stress was measured following Wu et al. (Yang et al., 2016) and presented in Fig. 9b. The HDI stress increased sharply at the initial stage of deformation, and then reached a stable stage gradually. This is because the interface may absorb some GND pileups and consequently do not contribute to HDI hardening with increasing strain gradient, consistent with the strain partitioning (Fig. 7) and previous findings (Wang et al., 2020). Comparing with single-phase heterostructured HEAs (Slone et al., 2019; Wu et al., 2019), the HDI stress is much higher, resulting in a more efficient strain hardening effect. This explained the high strain hardening rate of partially recrystallized $Ni_2CoCrFeTi_{0.24}Al_{0.2}$ and thus good ductility in Fig. 6. Compared with the partially recrystallized HEA, the non-recrystallized and fully recrystallized showed lower strain hardening capacity and ductility due to the absence of grain-scale heterogeneous structures (Fig. 1) (Wu et al., 2014; Zhu and Wu, 2019).

4.2. Strengthening mechanisms

As Fig. 6 demonstrated, the superior yield strength of ~1.3 GPa was obtained in partially recrystallized $Ni_2CoCrFeTi_{0.24}Al_{0.2}$. Complex microstructures in Figs. 1–5 revealed that such a high yield strength comes from a comprehensive strengthening of different metallurgy mechanisms. In previous studies, grain boundary and solid solution hardening contributions have been found relatively small by several groups (He et al., 2016, 2019; Tong et al., 2019). In the following, we therefore mainly discussed the precipitation hardening and dislocation strengthening, which are the main strengthening mechanisms that we aimed to unitize in the current HEAs. Since the ordering strengthening plays the dominant role in the precipitation hardening of all reported γ′-hardened HEAs (He et al., 2016; Ming et al., 2018; Zhao et al., 2017), we followed Ardell (1985), $\sigma_{or} = M0.81\frac{\gamma_{APB}}{2b}\left(\frac{3\pi f}{8}\right)^{1/2}$, to estimate the yield strength increase caused by precipitates. Here, the precipitation hardening effect is mainly determined by volume fraction (f) and anti-phase boundary (APB) energy (γ_{APB}) of the γ′ phase since M = 3.06 is the Taylor factor for polycrystalline FCC metals, and $b = \frac{\sqrt{2}}{2}a$ is the magnitude of the Burgers vector of the matrix. The volume fraction of the γ′ phase in the current study was measured to be ~30% from DF images in Fig. S4 and supported by the CALPAD simulation in Fig. S6. The particle sizes, which are defined as an average area-equivalent diameter ($d = 2\sqrt{area/\pi}$) in the current study, of the γ′ phase in different regions were also obtained from these DF images. At least three images were used for the measurement of volume fraction and particle size. The average value of ~30 nm was obtained to calculate the strengthening effect. The γ_{APB} of 0.18 J m^{-2} is adopted from the $Ni_2CoCrFeTi_{0.15}Al_{0.15}$ (He et al., 2021). From XRD patterns in Fig. 2b, the lattice parameter of the matrix is 0.3577 nm and thus b = 0.253 nm. Bringing these values into the above equation for ordering strengthening, we then obtained the yield strength increase from the γ′ phase is 524 MPa.

To make the estimation more convincing, we measured the precipitation hardening effect experimentally. Fig. 10a showed the stress-strain curves of the single-phase $Ni_2CoCrFe$ base HEA and the recrystallized and aged $Ni_2CoCrFeTi_{0.24}Al_{0.2}$. Their representative microstructures were shown in Fig. 10b. Here, both $Ni_2CoCrFe$ and $Ni_2CoCrFeTi_{0.24}Al_{0.2}$ were fully recrystallized, and the recrystallized $Ni_2CoCrFeTi_{0.24}Al_{0.2}$ HEA was further aged at 800 °C for 90 min to promote the precipitation of γ′ phase. The yield strengths of the $Ni_2CoCrFe$ matrix and precipitation hardened $Ni_2CoCrFeTi_{0.24}Al_{0.2}$ HEA are ~270 and ~790 MPa, respectively. The precipitation hardening effect can be roughly estimated to be 520 MPa by comparing the yield strengths of the $Ni_2CoCrFe$ base and recrystallized and aged $Ni_2CoCrFeTi_{0.24}Al_{0.2}$ HEAs, agreeing well with that estimated by ordering strengthening mechanism. The consistency between the experimentally and theoretically measured values allows us to safely conclude that the precipitates in the partially recrystallized $Ni_2CoCrFeTi_{0.24}Al_{0.2}$ HEA caused a yield strength increase by ~520 MPa.

Dislocation strengthening is widely described using the model of Taylor et al. (Argon, 2008), $\sigma_d = \sigma_0 + MG\alpha b\sqrt{\rho}$, where G is the shear modulus, α is a constant, and ρ is the dislocation density. However, it is not easy to quantify the dislocation density in metals by TEM or conventional XRD accurately. Here, we experimentally evaluated the dislocation strengthening by removing the precipitation

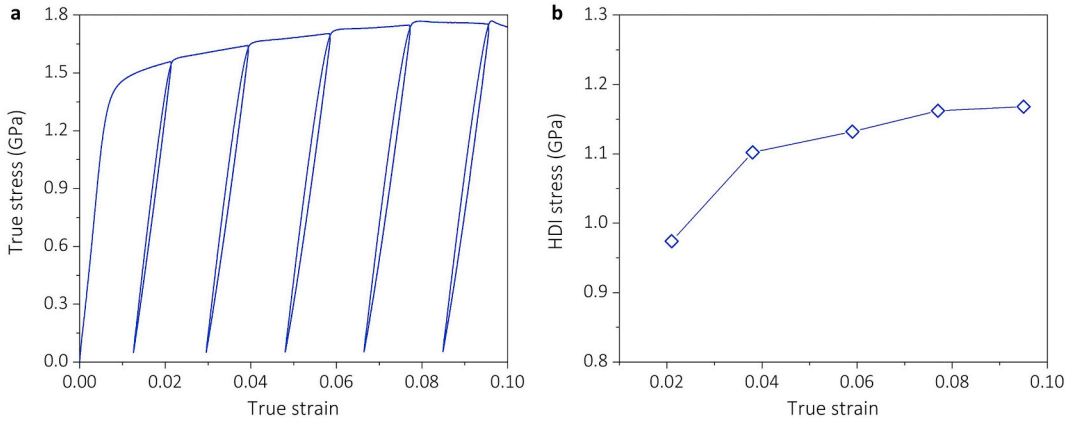

Fig. 9. (a) The load-unload-reload (LUR) test, (b) the HDI stress as a function of true strain of the partially recrystallized $Ni_2CoCrFeTi_{0.24}Al_{0.2}$ HEA.

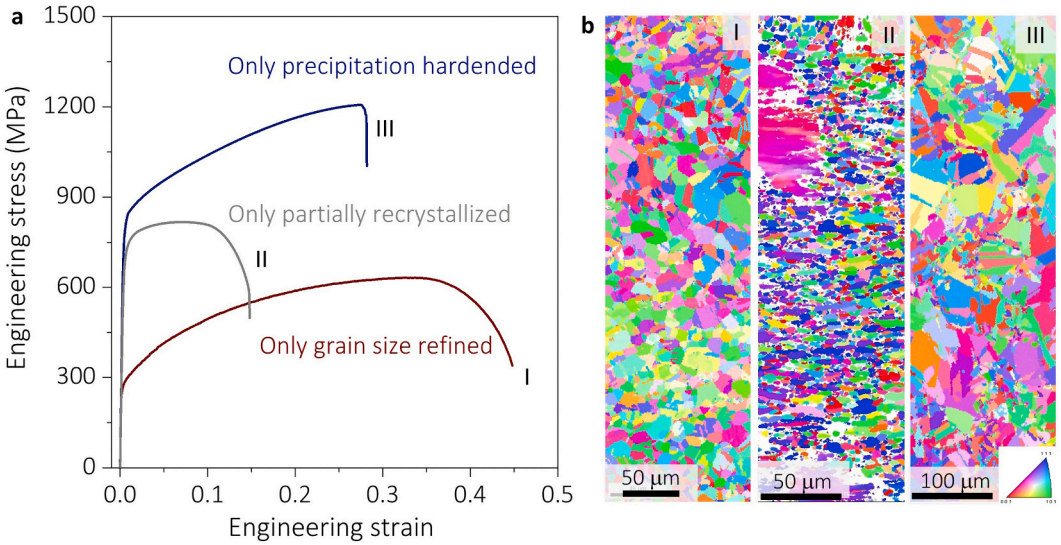

Fig. 10. (a) The tensile stress-strain curves of different HEAs, I - the fully recrystallized $Ni_2CoCrFe$, II – partially recrystallized $Ni_2CoCrFe$, III – fully recrystallized and aged $Ni_2CoCrFeTi_{0.24}Al_{0.2}$; (b) Corresponding IPF images of HEAs in (a).

effect in $Ni_2CoCrFe$. We note that the $Ni_2CoCrFe$, instead of the real matrix alloy with minor Ti and Al, was chosen to completely avoid precipitates at 800 °C because it has been reported that the solid solubility of Ti and Al in the NiCoCrFe HEA is very low and that the NiCoCrFe is metastable at intermediate temperatures (He et al., 2017, 2018a). $Ni_2CoCrFe$ was solutionized, then 70% cold-rolled, and finally partially recrystallized to simulate the dislocation state of partially recrystallized $Ni_2CoCrFeTi_{0.24}Al_{0.2}$. The stress-strain curves of the single-phase partially recrystallized base HEA (the gray curve in Fig. 10a). The representative microstructure with ~50% recrystallized area was given in Fig. 10b. Comparing the yield strengths of the partially (~690 MPa) and fully recrystallized $Ni_2CoCrFe$ (~270 MPa), we found that the dislocation strengthening contributed ~420 MPa to the yield strength of the partially recrystallized sample. Since the $Ni_2CoCrFeTi_{0.24}Al_{0.2}$ HEA was also cold-rolled in a single-phase state and its hardness at the cold-rolled state is similar to that of the $Ni_2CoCrFe$ HEA, we can roughly say that the dislocation strengthening effect in the partially recrystallized $Ni_2CoCrFeTi_{0.24}Al_{0.2}$ HEA is also close to ~420 MPa. Then the theoretical yield strength of partially $Ni_2CoCrFeTi_{0.24}Al_{0.2}$ is calculated to be 270 + 420 +520 = 1210 MPa. This value is slightly smaller than the experimental value of 1300 MPa. We suggest that this difference might come from the grain-boundary effect since the recrystallized grains of $Ni_2CoCrFeTi_{0.24}Al_{0.2}$ (Fig. 1b) are much smaller than that of the $Ni_2CoCrFe$ (Fig. 10b). Despite some simplification in the strengthening analysis, we can still conclude that the precipitation and dislocation hardening are the main origins of the excellent yield strength of the partially $Ni_2CoCrFeTi_{0.24}Al_{0.2}$ HEA.

5. Conclusion

In summary, we in the current study developed a $Ni_2CoCrFeTi_{0.24}Al_{0.2}$ HEA with grain-scale heterogeneous structure and nano-sized γ' phase using a facile processing route. The resulted microstructure simultaneously achieved ultra-high strength and excellent ductility. With the aid of SEM, XRD, EBSD, TEM, and micro-DIC analysis, the origins of the excellent mechanical properties were revealed. The major conclusions were presented in the following.

- Through single-step rolling and annealing, a $Ni_2CoCrFeTi_{0.24}Al_{0.2}$ HEA with an excellent strength-ductility combination was developed. The novel HEA exhibits grain-scale heterogeneous structure together with stable γ' precipitates with particle size ranging from ~10 to ~100 nm. This heterogeneous precipitated microstructure led to a yield strength of ~1.3 GPa, tensile strength of ~1.5 GPa, and tensile elongation of ~20%.
- Micro-DIC analysis revealed that the heterogeneous structure caused strong strain partitioning during tensile deformation, stimulating additional deformation mechanisms and efficient HDI strain hardening. Apart from abundant SFs as observed in previous studies, deformation twins and micro-bands were frequently observed in the large-grain and non-recrystallized regions, respectively. These additional deformation modes, together with high HDI stress of ~1–1.2 GPa, resulted in the good ductility of the heterogeneous precipitated $Ni_2CoCrFeTi_{0.24}Al_{0.2}$ HEA.
- Based on the quantified microstructure analysis and experimental validation, we attributed the high yield strength of the partially recrystallized $Ni_2CoCrFeTi_{0.24}Al_{0.2}$ HEA mainly to precipitation hardening and dislocation hardening, which contributed ~520 and ~420 MPa, respectively. These outcomes provide an economical and efficient path to develop ultra-strong and ductile materials and deepen the understanding of the deformation mechanism of heterogeneous structures as well.

CRediT authorship contribution statement

Feng He: Conceptualization, Methodology, Investigation, Writing – review & editing. **Zhongsheng Yang:** Investigation, Validation. **Shaofei Liu:** Investigation, Validation. **Da Chen:** Investigation, Validation. **Weitong Lin:** Writing – review & editing. **Tao Yang:** Writing – review & editing. **Daixiu Wei:** Writing – review & editing. **Zhijun Wang:** Supervision, Reviewing, Funding acquisition. **Jincheng Wang:** and. **Ji-jung Kai:** Supervision, Funding acquisition.

Declaration of competing interest

The authors declare that they have no known competing financial interests or personal relationships that could have appeared to influence the work reported in this paper.

Acknowledgments

The authors are grateful for the financial support from the Hong Kong Research Grant Council (JJK, Hong Kong Grant No. CityU 11212915 and CityU 11205018), National Natural Science Foundation of China (ZJW, Grant No. 51771149 and FH Grant No. 52001266).

Appendix A. Supplementary data

Supplementary data to this article can be found online at https://doi.org/10.1016/j.ijplas.2021.103022.

References

Ardell, A.J., 1985. Precipitation hardening. Metallurgical Transactions A 16, 2131–2165.
Argon, A., 2008. Strengthening Mechanisms in Crystal Plasticity. Oxford University Press on Demand.
Bay, B., Hansen, N., Hughes, D.A., Kuhlmann-Wilsdorf, D., 1992. Overview no. 96 evolution of f.c.c. deformation structures in polyslip. Acta Metall. Mater. 40, 205–219.
Chen, D., He, F., Han, B., Wu, Q., Tong, Y., Zhao, Y., Wang, Z., Wang, J., Kai, J.-j., 2019. Synergistic effect of Ti and Al on L12-phase design in CoCrFeNi-based high entropy alloys. Intermetallics 110, 106476.
Chung, D., Ding, Z., Yang, Y., 2019. Hierarchical eutectic structure enabling superior fracture toughness and superb strength in CoCrFeNiNb0.5 eutectic high entropy alloy at room temperature. Adv. Eng. Mater. 21, 1801060.
Du, X.H., Li, W.P., Chang, H.T., Yang, T., Duan, G.S., Wu, B.L., Huang, J.C., Chen, F.R., Liu, C.T., Chuang, W.S., Lu, Y., Sui, M.L., Huang, E.W., 2020. Dual heterogeneous structures lead to ultrahigh strength and uniform ductility in a Co-Cr-Ni medium-entropy alloy. Nat. Commun. 11, 2390.
Fan, L., Yang, T., Zhao, Y., Luan, J., Zhou, G., Wang, H., Jiao, Z., Liu, C.-T., 2020. Ultrahigh strength and ductility in newly developed materials with coherent nanolamellar architectures. Nat. Commun. 11, 6240.
George, E.P., Curtin, W.A., Tasan, C.C., 2020. High entropy alloys: a focused review of mechanical properties and deformation mechanisms. Acta Mater. 188, 435–474.
George, E.P., Raabe, D., Ritchie, R.O., 2019. High-entropy alloys. Nature Reviews Materials 4, 515–534.
Gludovatz, B., Hohenwarter, A., Catoor, D., Chang, E.H., George, E.P., Ritchie, R.O., 2014. A fracture-resistant high-entropy alloy for cryogenic applications. Science 345, 1153–1158.
Han, B., Wei, J., Tong, Y., Chen, D., Zhao, Y., Wang, J., He, F., Yang, T., Zhao, C., Shimizu, Y., Inoue, K., Nagai, Y., Hu, A., Liu, C.T., Kai, J.J., 2018. Composition evolution of gamma prime nanoparticles in the Ti-doped CoFeCrNi high entropy alloy. Scripta Mater. 148, 42–46.
Hasan, M.N., Liu, Y.F., An, X.H., Gu, J., Song, M., Cao, Y., Li, Y.S., Zhu, Y.T., Liao, X.Z., 2019. Simultaneously enhancing strength and ductility of a high-entropy alloy via gradient hierarchical microstructures. Int. J. Plast. 123, 178–195.
He, F., Chen, D., Han, B., Wu, Q., Wang, Z., Wei, S., Wei, D., Wang, J., Liu, C.T., Kai, J.-j., 2019. Design of D022 superlattice with superior strengthening effect in high entropy alloys. Acta Mater. 167, 275–286.
He, F., Han, B., Yang, Z., Chen, D., Yeli, G., Tong, Y., Wei, D., Li, J., Wang, Z., Wang, J., Kai, J.-j., 2021. Elemental partitioning as a route to design precipitation-hardened high entropy alloys. J. Mater. Sci. Technol. 72, 52–60.
He, F., Wang, Z., Han, B., Wu, Q., Chen, D., Li, J., Wang, J., Liu, C.T., Kai, J.J., 2018a. Solid solubility, precipitates, and stacking fault energy of micro-alloyed CoCrFeNi high entropy alloys. J. Alloys Compd. 769, 490–502.
He, F., Wang, Z., Wu, Q., Chen, D., Yang, T., Li, J., Wang, J., Liu, C.T., Kai, J.-j., 2018b. Tuning the defects in face centered cubic high entropy alloy via temperature-dependent stacking fault energy. Scripta Mater. 155, 134–138.
He, F., Wang, Z., Wu, Q., Li, J., Wang, J., Liu, C.T., 2017. Phase separation of metastable CoCrFeNi high entropy alloy at intermediate temperatures. Scripta Mater. 126, 15–19.
He, J.Y., Wang, H., Huang, H.L., Xu, X.D., Chen, M.W., Wu, Y., Liu, X.J., Nieh, T.G., An, K., Lu, Z.P., 2016. A precipitation-hardened high-entropy alloy with outstanding tensile properties. Acta Mater. 102, 187–196.
He, Y., Yang, H., Zhao, C., Zhang, Y., Pan, X., Li, J., Wang, J., 2020. Enhancing mechanical properties of Al0.25CoCrFeNi high-entropy alloy via cold rolling and subsequent annealing. J. Alloys Compd. 830, 154645.
Hou, J., Wang, Z., Shi, X., Wang, Z., Qiao, J., Wu, Y., 2020. Strengthening of an Al0.45CoCrFeNi high-entropy alloy via in situ fabricated duplex-structured composites. J. Mater. Sci. 55, 7894–7909.
Hua, N., Wang, W., Wang, Q., Ye, Y., Lin, S., Zhang, L., Guo, Q., Brechtl, J., Liaw, P.K., 2021. Mechanical, corrosion, and wear properties of biomedical Ti–Zr–Nb–Ta–Mo high entropy alloys. J. Alloys Compd. 861, 157997.
Jo, Y.H., Jung, S., Choi, W.M., Sohn, S.S., Kim, H.S., Lee, B.J., Kim, N.J., Lee, S., 2017. Cryogenic strength improvement by utilizing room-temperature deformation twinning in a partially recrystallized VCrMnFeCoNi high-entropy alloy. Nat. Commun. 8, 15719.
Laplanche, G., Kostka, A., Reinhart, C., Hunfeld, J., Eggeler, G., George, E.P., 2017. Reasons for the superior mechanical properties of medium-entropy CrCoNi compared to high-entropy CrMnFeCoNi. Acta Mater. 128, 292–303.
Li, J., Chen, H., Fang, Q., Jiang, C., Liu, Y., Liaw, P.K., 2020a. Unraveling the dislocation–precipitate interactions in high-entropy alloys. Int. J. Plast. 133, 102819.
Li, J., Lu, W., Chen, S., Liu, C., 2020b. Revealing extra strengthening and strain hardening in heterogeneous two-phase nanostructures. Int. J. Plast. 126, 102626.

Li, Y., Li, L., Gao, X., Zhang, W., Lin, X., Xue, J., Zhang, G., 2020c. Research progress on refractory high entropy alloys. Rare Met. Mater. Eng. 49, 4365–4372.
Li, Z., Tasan, C.C., Pradeep, K.G., Raabe, D., 2017. A TRIP-assisted dual-phase high-entropy alloy: grain size and phase fraction effects on deformation behavior. Acta Mater. 131, 323–335.
Liu, W.H., Lu, Z.P., He, J.Y., Luan, J.H., Wang, Z.J., Liu, B., Liu, Y., Chen, M.W., Liu, C.T., 2016. Ductile CoCrFeNiMox high entropy alloys strengthened by hard intermetallic phases. Acta Mater. 116, 332–342.
Liu, W.H., Wu, Y., He, J.Y., Nieh, T.G., Lu, Z.P., 2013. Grain growth and the Hall–Petch relationship in a high-entropy FeCrNiCoMn alloy. Scripta Mater. 68, 526–529.
Liu, Y., Cao, Y., Mao, Q., Zhou, H., Zhao, Y., Jiang, W., Liu, Y., Wang, J.T., You, Z., Zhu, Y., 2020. Critical microstructures and defects in heterostructured materials and their effects on mechanical properties. Acta Mater. 189, 129–144.
Ma, E., Wu, X., 2019. Tailoring heterogeneities in high-entropy alloys to promote strength-ductility synergy. Nat. Commun. 10, 5623.
Ma, Y., Yuan, F., Yang, M., Jiang, P., Ma, E., Wu, X., 2018. Dynamic shear deformation of a CrCoNi medium-entropy alloy with heterogeneous grain structures. Acta Mater. 148, 407–418.
Ming, K., Bi, X., Wang, J., 2017. Precipitation strengthening of ductile Cr 15 Fe 20 Co 35 Ni 20 Mo 10 alloys. Scripta Mater. 137, 88–93.
Ming, K., Bi, X., Wang, J., 2018. Realizing strength-ductility combination of coarse-grained Al0.2Co1.5CrFeNi1.5Ti0.3 alloy via nano-sized, coherent precipitates. Int. J. Plast. 100, 177–191.
Miracle, D.B., Senkov, O.N., 2017. A critical review of high entropy alloys and related concepts. Acta Mater. 122, 448–511.
Nandal, V., Sarvesha, R., Singh, S.S., Huang, E.W., Chang, Y.-J., Yeh, A.-C., Neelakantan, S., Jain, J., 2021. Influence of pre-deformation on the precipitation characteristics of aged non-equiatomic Co1.5CrFeNi1.5 high entropy alloys with Ti and Al additions. J. Alloys Compd. 855, 157521.
Niendorf, T., Rüsing, C.J., Frehn, A., Maier, H.J., 2013. The deformation behavior of functionally graded TWIP steel under monotonic loading at ambient temperature. Materials Research Letters 1, 96–101.
Sadeghilaridjani, M., Ayyagari, A., Muskeri, S., Hasannaeimi, V., Salloom, R., Chen, W.-Y., Mukherjee, S., 2020. Ion irradiation response and mechanical behavior of reduced activity high entropy alloy. J. Nucl. Mater. 529, 151955.
Schneider, M., George, E.P., Manescau, T.J., Záležák, T., Hunfeld, J., Dlouhý, A., Eggeler, G., Laplanche, G., 2020. Analysis of strengthening due to grain boundaries and annealing twin boundaries in the CrCoNi medium-entropy alloy. Int. J. Plast. 124, 155–169.
Slone, C.E., Miao, J., George, E.P., Mills, M.J., 2019. Achieving ultra-high strength and ductility in equiatomic CrCoNi with partially recrystallized microstructures. Acta Mater. 165, 496–507.
Slone, C.E., Miao, J., Mills, M.J., 2018. Ultra-high strength and ductility from rolling and annealing of a Ni-Cr-Co superalloy. Scripta Mater. 155, 94–98.
Sohn, S.S., Song, H., Jo, M.C., Song, T., Kim, H.S., Lee, S., 2017. Novel 1.5 GPa-strength with 50%-ductility by transformation-induced plasticity of non-recrystallized austenite in duplex steels. Sci. Rep. 7, 1255.
Su, J., Raabe, D., Li, Z., 2019. Hierarchical microstructure design to tune the mechanical behavior of an interstitial TRIP-TWIP high-entropy alloy. Acta Mater. 163, 40–54.
Sunkari, U., Reddy, S.R., Rathod, B.D.S., Kumar, S.S.S., Saha, R., Chatterjee, S., Bhattacharjee, P.P., 2020. Heterogeneous precipitation mediated heterogeneous nanostructure enhances strength-ductility synergy in severely cryo-rolled and annealed CoCrFeNi2.1Nb0.2 high entropy alloy. Sci. Rep. 10, 6056.
Toda-Caraballo, I., Rivera-Díaz-del-Castillo, P.E.J., 2015. Modelling solid solution hardening in high entropy alloys. Acta Mater. 85, 14–23.
Tong, Y., Chen, D., Han, B., Wang, J., Feng, R., Yang, T., Zhao, C., Zhao, Y.L., Guo, W., Shimizu, Y., Liu, C.T., Liaw, P.K., Inoue, K., Nagai, Y., Hu, A., Kai, J.J., 2019. Outstanding tensile properties of a precipitation-strengthened FeCoNiCrTi0.2 high-entropy alloy at room and cryogenic temperatures. Acta Mater. 165, 228–240.
Wang, Y.F., Huang, C.X., Fang, X.T., Höppel, H.W., Göken, M., Zhu, Y.T., 2020. Hetero-deformation induced (HDI) hardening does not increase linearly with strain gradient. Scripta Mater. 174, 19–23.
Wei, S., He, F., Tasan, C.C., 2018. Metastability in high-entropy alloys: a review. J. Mater. Res. 33, 2924–2937.
Wei, S., Kim, J., Tasan, C.C., 2019. Boundary micro-cracking in metastable Fe45Mn35Co10Cr10 high-entropy alloys. Acta Mater. 168, 76–86.
Wu, S.W., Wang, G., Wang, Q., Jia, Y.D., Yi, J., Zhai, Q.J., Liu, J.B., Sun, B.A., Chu, H.J., Shen, J., Liaw, P.K., Liu, C.T., Zhang, T.Y., 2019. Enhancement of strength-ductility trade-off in a high-entropy alloy through a heterogeneous structure. Acta Mater. 165, 444–458.
Wu, X., Jiang, P., Chen, L., Yuan, F., Zhu, Y.T., 2014. Extraordinary strain hardening by gradient structure. Proc. Natl. Acad. Sci. U. S. A. 111, 7197–7201.
Yang, M., Pan, Y., Yuan, F., Zhu, Y., Wu, X., 2016. Back stress strengthening and strain hardening in gradient structure. Materials Research Letters 4, 145–151.
Yang, M., Yan, D., Yuan, F., Jiang, P., Ma, E., Wu, X., 2018a. Dynamically reinforced heterogeneous grain structure prolongs ductility in a medium-entropy alloy with gigapascal yield strength. Proc. Natl. Acad. Sci. U. S. A. 115, 7224–7229.
Yang, T., Zhao, Y.L., Tong, Y., Jiao, Z.B., Wei, J., Cai, J.X., Han, X.D., Chen, D., Hu, A., Kai, J.J., Lu, K., Liu, Y., Liu, C.T., 2018b. Multicomponent intermetallic nanoparticles and superb mechanical behaviors of complex alloys. Science 362, 933–937.
Yoo, J.D., Park, K.-T., 2008. Microband-induced plasticity in a high Mn–Al–C light steel. Mater. Sci. Eng., A 496, 417–424.
Zhang, B.B., Yan, F.K., Zhao, M.J., Tao, N.R., Lu, K., 2018. Combined strengthening from nanotwins and nanoprecipitates in an iron-based superalloy. Acta Mater. 151, 310–320.
Zhang, C., Zhu, C., Cao, P., Wang, X., Ye, F., Kaufmann, K., Casalena, L., MacDonald, B.E., Pan, X., Vecchio, K., Lavernia, E.J., 2020a. Aged metastable high-entropy alloys with heterogeneous lamella structure for superior strength-ductility synergy. Acta Mater. 199, 602–612.
Zhang, T.W., Ma, S.G., Zhao, D., Wu, Y.C., Zhang, Y., Wang, Z.H., Qiao, J.W., 2020b. Simultaneous enhancement of strength and ductility in a NiCoCrFe high-entropy alloy upon dynamic tension: micromechanism and constitutive modeling. Int. J. Plast. 124, 226–246.
Zhang, Y., Zuo, T.T., Tang, Z., Gao, M.C., Dahmen, K.A., Liaw, P.K., Lu, Z.P., 2014. Microstructures and properties of high-entropy alloys. Prog. Mater. Sci. 61, 1–93.
Zhao, J., Lu, X., Yuan, F., Kan, Q., Qu, S., Kang, G., Zhang, X., 2020. Multiple mechanism based constitutive modeling of gradient nanograined material. Int. J. Plast. 125, 314–330.
Zhao, Y.L., Yang, T., Tong, Y., Wang, J., Luan, J.H., Jiao, Z.B., Chen, D., Yang, Y., Hu, A., Liu, C.T., Kai, J.J., 2017. Heterogeneous precipitation behavior and stacking-fault-mediated deformation in a CoCrNi-based medium-entropy alloy. Acta Mater. 138, 72–82.
Zheng, T., Hu, X., He, F., Wu, Q., Han, B., Chen, D., Li, J., Wang, Z., Wang, J., Kai, J.-j., Xia, Z., Liu, C.T., 2021. Tailoring nanoprecipitates for ultra-strong high-entropy alloys via machine learning and prestrain aging. J. Mater. Sci. Technol. 69, 156–167.
Zhu, Y., Wu, X., 2019. Perspective on hetero-deformation induced (HDI) hardening and back stress. Materials Research Letters 7, 393–398.